Research Article | Vol. 28, No. 25 / 7 December 2020 / Optics Express 37436
Optics EXPRESS

Experimental investigation of the jet-on-jet physical phenomenon in laser-induced forward transfer (LIFT)

JUSTINAS MIKŠYS,[1,2,*] GARI ARUTINOV,[2] MATTHIAS FEINAEUGLE,[1] AND GERT-WILLEM RÖMER[1]

[1] *Chair of Laser Processing, Department of Mechanics of Solids, Surfaces & Systems (MS3), Faculty of Engineering Technology, University of Twente, Drienerlolaan 5, 7522NB Enschede, The Netherlands*
[2] *Holst Centre/TNO, High Tech Campus 31, 5656AE Eindhoven, The Netherlands*
[*] *j.miksys@utwente.nl*

Abstract: Understanding the physics behind the ejection dynamics in laser-induced forward transfer (LIFT) is of key importance in order to develop new printing techniques and overcome their limitations. In this work, a new jet-on-jet ejection phenomenon is presented and its physical origin is discussed. Time-resolved shadowgraphy imaging was employed to capture the ejection dynamics and is complemented with the photodiode intensity measurements in order to capture the light emitted by laser-induced plasma. A focus scan was conducted, which confirmed that the secondary jet is ejected due to laser-induced plasma generated at the center of the laser spot, where intensity is the highest. Five characteristic regions of the focus scan, with regards to laser fluence level and laser spot size, were distinguished. The study provides new insights in laser-induced jet dynamics and shows the possibility of overcoming the trade-off between the printing resolution and printing distance.

1. Introduction

Laser-induced forward transfer (LIFT) is a direct-write technique, where a (ultra)short pulsed and focused laser beam is employed to deposit a small amount of the donor material onto the target (*receiver*) substrate [1,2]. The donor material is coated on the bottom of a glass substrate (*carrier*), the latter being transparent to the wavelength of the laser source. The carrier and the receiver are spaced at a distance from each other, which here typically ranges from tenths of micrometers to a few millimeters enabling contactless printing. Combining a pulsed laser source with a galvanometer scanner allows LIFT to be a digital technique, where printing speed is characterized by the repetition rate of the laser source and can range up to millions deposits per second [3]. Furthermore, it has been recently demonstrated that a continuous wave (CW) laser source can also be used as a cost-effective alternative to (ultra)short pulsed laser sources [4].

A significant advantage of LIFT over other additive manufacturing techniques is its ability to deposit a large variety of materials. Successful LIFT printing of pure metals [5–7], ceramics [8–10], polymers [11,12], liquids [13–15], and even biomaterials [16,17] has been demonstrated. LIFT of silver particle-based inks and pastes, which are widely used as conductive materials in the field of printed electronics, have been successfully demonstrated as well [18–20]. LIFT of silver pastes for flexible electronics applications [21,22] for 2D as well as 3D interconnections has been shown on a laboratory scale [23,24]. However, in order to scale it up to industrial production rates, more fundamental understanding on the printing process and the role of the governing processing parameters (material and laser) is needed.

The LIFT process is determined by multiple variables, including laser parameters (such as laser wavelength, spot size, (pulse) energy, pulse duration, etc.), optics (e.g. numerical aperture of the lens), material to be printed (chemical composition, phase, thickness, viscosity, uniformity, etc.)

#401825 https://doi.org/10.1364/OE.401825
Journal © 2020 Received 2 Jul 2020; revised 6 Oct 2020; accepted 6 Oct 2020; published 30 Nov 2020

Optics EXPRESS

and alignment of carrier to receiver substrate (e.g. printing distance). The processing window, where controlled and reproducible jetting of the donor material is obtained is typically narrow [25–27]. A stroboscopic shadowgraphy imaging technique is commonly applied [3,19,20,26,28] to facilitate understanding of LIFT jetting dynamics, as well as to ease the parameter optimization process. Such time-resolved studies revealed that, in LIFT of silver nanoparticle inks, the absorbed laser energy induces a cavitation bubble at the carrier/donor interface, due to the rapid vaporization of the solvent [29,30]. This laser-induced bubble thrusts the donor material (ink) away from the carrier substrate and expands until the evaporated solvent pressure inside the bubble becomes lower than the outside (atmospheric) pressure. At this instance the bubble starts to collapse into a single jet, with its width reducing as the jet elongates [30,31].

In this study, we present and discuss a 'jet-on-jet' ejection mechanism, where a smaller secondary jet forms on top of the main, larger jet. To the authors knowledge, this jet-on-jet phenomenon has not been reported before, as all previous works study dynamics of a single jet, induced by a single ejection mechanism. This paper focuses on the role of the laser processing parameters, such as pulse energy, spot size and fluence, in the formation of the secondary jet. Complementary to the shadowgraphy imaging, which is widely used to capture LIFT dynamics, detection of the laser-induced plasma emission by photodiodes was used in order to understand the impact of the laser-induced plasma to the jet-on-jet phenomenon. The jet-on-jet phenomenon shows a potential of printing small(er) deposits over a larger printing distance, compared to what is feasible with conventional, single jets.

2. Materials and methods

Figure 1 schematically shows the laser setup, as well as the time-resolved shadowgraphy imaging setup used to capture the evolution of LIFT jets. A frequency tripled ($\lambda = 355$ nm) Nd:YAG laser AVIA-355-4500 (Coherent, Germany) with pulse duration $\tau_{FWHM} = 30$ ns, maximum pulse energy $E_p = 200$ µJ and Gaussian intensity profile ($M^2 < 1.3$) was used. The laser beam was focused using a $f = 100$ mm focal length plano-convex lens (Thorlabs GmbH, Germany), producing a $2\omega_0 = 17 \pm 2$ µm diameter laser focal spot. A frequency doubled ($\lambda = 532$ nm) Nd:YVO_4 laser source AOT-YVO-1 SP (InnoLas, Germany) with pulse duration $\tau_{FWHM} = 80$ ps was used to excite the fluorescent rhodamine 6G dye. Light, emitted by rhodamine, was used to illuminate the ejection phenomena, which was captured by a Prosilica GC1380 charge-coupled device (CCD) camera (Allied Vision, Germany).

Full temporal jet evolutions were collected by varying the delay time between the LIFT laser pulse and the pulse from the illumination source, using a delay generator, while the shutter of the CCD camera was kept open during the complete process of the ejection. Complementary to the shadowgraphy imaging, a pair of photodiodes (PD1 and PD2) were used in order to capture the light, emitted by the laser source (PD1) and light emitted from the donor/laser interaction volume (PD2), see Fig. 1. Photodiode (PD1) was used to capture light which was partly reflected (R ≈ 4%) from the glass slide (GS). This photodiode signal was used as a reference to time the response of the second photodiode. The second photodiode (PD2) was used to capture the light emitted from the laser-material interaction volume. In order to efficiently collect the emitted light a $f = 25$ mm focal length plano-convex lens was used, combined with a 400 nm longpass optical filter to reduce the effect of scattered laser light on the signal of PD2. The rise time of both photodiodes was 1 ns.

Silver nanoparticle ink with 75 wt % metal content [32] was blade coated on the 0.7 mm thick soda-lime glass carrier plate and used as a donor material. All experiments were conducted using a donor layer thickness of $h_D = 120 \pm 2$ µm right after the coating process, so the evaporation of the solvent would not have an impact.

After the LIFT experiments, the donor material was removed from the carrier and the carrier surface was examined using optical BX51 (Olympus GmbH, Germany) and confocal Leica DCM

Optics EXPRESS

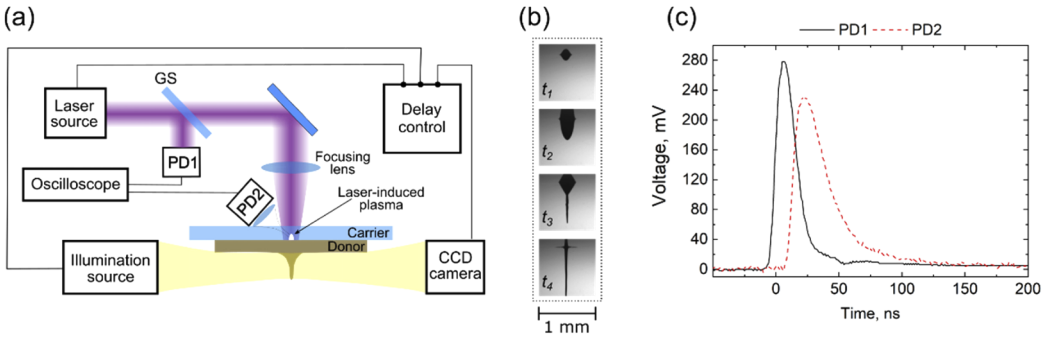

Fig. 1. (a) Schematic illustration of the laser- and time-resolved shadowgraphy imaging setup. A delay generator controls the delay between the start of the LIFT laser pulse and the start of the illumination laser pulse, in order to capture the full evolution of the LIFT ejection phenomena in a stroboscopic approach. A photodiode (PD2), combined with a lens is applied to capture the light emitted from the laser-material interaction volume. (b) Example images of the evolution of a LIFT jet at four different time instants (t_1-t_4), captured by the shadowgraphy imaging setup. (c) Emitted laser radiation captured by photodiode PD1, as function of time, as well as light emitted by the process, captured by photodiode PD2, as function of time.

3D (Leica MICROSYSTEMS, Germany) microscopes. Confocal microscope was also used in order to measure the donor layer thickness.

3. Results and discussion

The formation of a single jet during the LIFT process consists of three main stages, see Fig. 2(a). In the first stage a high pressure laser-induced vapor bubble expands. Expansion continues until the pressure inside the bubble becomes lower than outside (atmospheric) pressure. Once this state is reached, the second stage starts in which the bubble starts to collapse—i.e. the width of the bubble decreases, inducing the silver ink flow from the sides to the center, forming a jet. Once the bubble is collapsed and the jet is fully formed, the third stage starts during which the jet elongates. A detailed description of the LIFT ejection dynamics can be found in our previous work [33]. Figure 2(a) shows a shadowgraphy image sequence, taken from our previous study, of a typical single LIFT jet formation, highlighting the three main stages mentioned above. Here the laser pulse with pulse energy of $E_p = 10.1 \pm 0.5$ µJ was focused to a waist diameter of $2\omega_0 = 80 \pm 3$ µm corresponding to a peak fluence of $F_0 = 0.40 \pm 0.05$ J/cm^2. In this case a relatively thin (35 ± 2 µm) donor layer was used, which resulted in final jet length of about 700 µm. In order to cover larger (than 700 µm) printing distances, the donor layer thickness has to be increased. As the donor layer thickness increases, larger laser spot diameters and higher laser fluence levels are required in order to thrust the donor material away from the carrier substrate and generate a stable jet.

Figure 2(b) shows LIFT jets, ejected from a 120 ± 3 µm thick donor layer, using a laser pulse energy of $E_p = 200 \pm 2$ µJ and a $2\omega = 250 \pm 5$ µm diameter spot ($F_0 = 0.8 \pm 0.1$ J/cm^2) at the carrier-donor interface. Here, a smaller secondary jet, forming at the front of the main ejection can be observed. Hence the naming *jet-on-jet*. Figure 2(c) shows the same ejection sequence, but the images are zoomed to the smaller secondary jet only. From this latter sequence it can be observed that the evolution of the smaller secondary jet follows the same three stages as the "classical" single jet, shown in Fig. 2(a). However, the dynamics of the main and the secondary jets, shown in Fig. 2(b), are not synchronized in time. That is, the collapse stage of the secondary

Optics EXPRESS

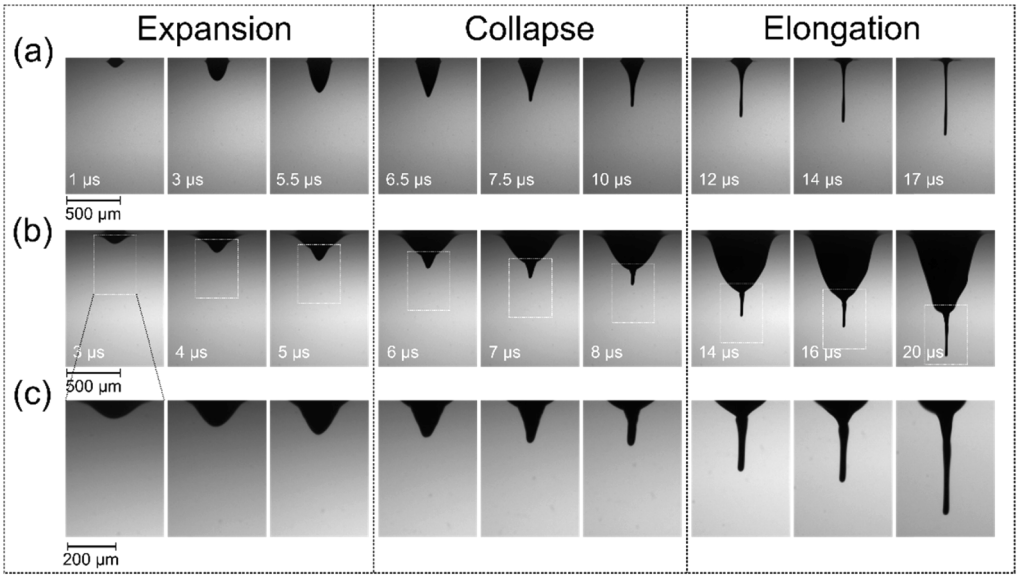

Fig. 2. Time-resolved shadowgraphy images of LIFT jet formation. Times are indicating the delay. The top of each frame of the images is placed at the carrier-donor interface. (a) Formation of a single jet; laser pulse energy $E_p = 10$ µJ and beam waist diameter $2\omega = 80$ µm corresponds to peak fluence of $F_0 = 0.4$ J/cm^2, donor layer thickness $h_D = 35$ µm; (b) Formation of a jet-on-jet, where laser pulse energy $E_p = 200$ µJ and beam waist diameter $2\omega = 250$ µm corresponds to a peak fluence of $F_0 = 0.8$ J/cm^2, donor layer thickness $h_D = 120$ µm; (c) Formation of jet-on-jet of graph (b), but zoomed on the secondary jet only.

jet takes place from 6 µs to 8 µs, while the main ejection starts collapsing later, around 16 µs. This indicates that the physical origin of these two jets is most likely different.

In order to understand how the main processing parameters (spot size and fluence level) affect the jet-on-jet formation, a "focus scan" was conducted. That is, at fixed pulse energy of $E_p = 200 \pm 4$ µJ the focal position of the laser beam was varied from $z = -7$ mm (negative values represent the beam waist being below the carrier/donor interface) to $z = +7$ mm, where $z = 0$ mm represents the beam focal spot exactly on top of the donor layer. The range of positions of the focus spot implied that the laser beam diameter on the donor surface varied from 550 µm (at $z = \pm 7$ mm) to 17 µm (at $z = 0$ mm). This corresponds to peak fluence levels ranging from 0.17 J/cm^2 to 176 J/cm^2, respectively. As the silver content of the used ink is relatively high (75% wt., see previous section), the optical penetration depth of the laser radiation into the ink is in the range of hundreds of nanometers. Therefore, when compared to the thickness of the donor layer (120 ± 2 µm, see previous section) we can assume that the laser energy is absorbed within a thin layer of the donor and no bulk absorption of laser energy in the ink occurs.

It is well known that free electron absorption in metals is responsible for their rather low ablation and laser-induced plasma ignition thresholds [34,35]. It has been shown in laser-induced breakdown spectroscopy (LIBS) studies that silver nanoparticle-based targets exhibit even lower plasma ignition threshold than the bulk silver targets, and can range below 0.5 J/cm^2 using nanosecond laser pulses [36,37]. Since in our study the peak fluence values for most of the focal positions are above 0.5 J/cm^2, laser-induced plasma is most likely to be generated during the process. In order to establish whether plasma plays a role in the small(er) secondary jet formation, photodiode PD2 was used in order to capture the light emitted by the laser-induced plasma. An example of laser-induced plasma emission captured by photodiode PD2, as function of time, is

Optics EXPRESS

shown in Fig. 1(c). If laser-induced plasma was responsible for the secondary jet generation, the short life-time of the plasma (50-100 ns, see Fig. 1(c)) could explain a quick collapse of the secondary jet, compared to the main ejection, caused by the gas bubble expansion, occurring on a longer time scale, see Fig. 2(b). However, besides the laser-induced plasma, other physical processes could be responsible for the emission of the light from the laser-material interaction zone, such as black body radiation or fluorescence from the laser-carrier interaction volume. Since the photodiode signal does not provide spectral data, in order to distinguish these light emission effects, the focus scan was conducted using three sample configurations: (*a*) the usual LIFT configuration, where laser-donor interaction volume is spatially confined by the carrier above the donor, see Fig. 3(a); (*b*) a donor-up configuration, where the laser-donor interaction zone is "open" above the donor, see Fig. 3(b); and (*c*) a carrier-only configuration, where no donor material is present and the laser beam interacts with the carrier substrate only, see Fig. 3(c). For every configuration, the focal spot position $z = 0$ was chosen such that focal spot is exactly on top of the donor, in the case of configuration (b), and at the bottom of the carrier, in the case of configuration (a) and (c), see Fig. 3.

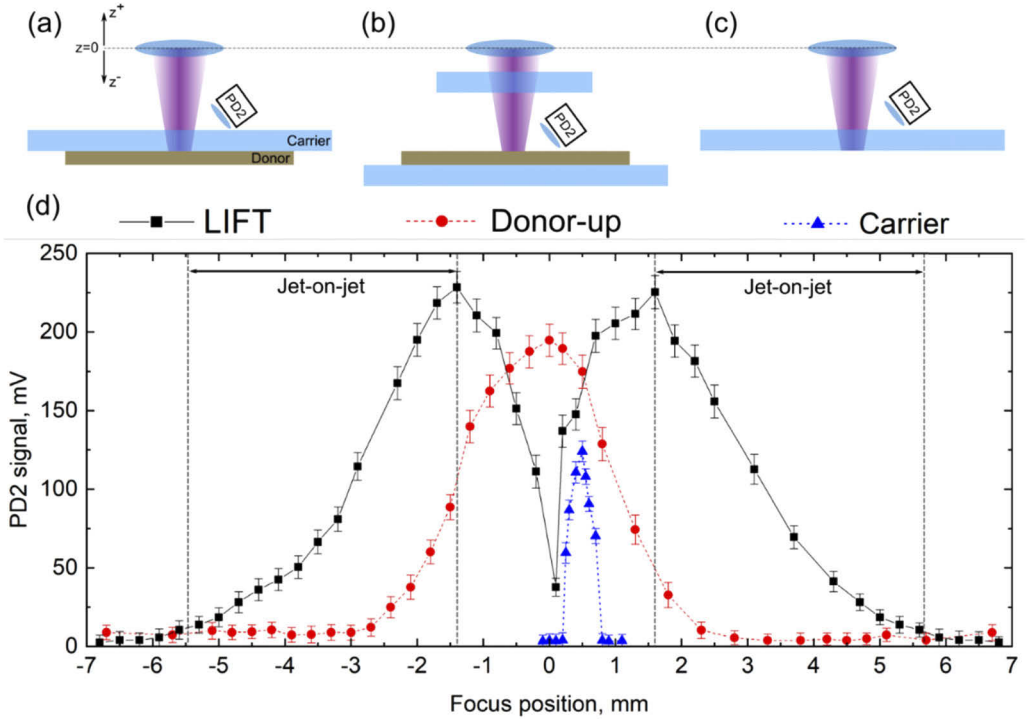

Fig. 3. Schematic illustration of the emitted light detection using the broad band photodiode (PD2) setup in (a) LIFT (b) donor-up and (c) carrier sample configurations; (d) the maximum signal captured by photodiode PD2 as function of on the position of the focal spot. The vertical dashed lines indicate the range where jet-on-jet effect is present.

The maximum of the captured light signal of PD2 as function of the focus position is shown in Fig. 3(d) for all three sample configurations. It can be observed from this graph, that the light emitted from the carrier (blue triangles) occurs only in the narrow range of focal positions – from $z = 0.2$ mm (focal spot inside the carrier) mm to $z = 0.8$ mm (focal spot slightly above the top surface of the carrier). Figure 4 shows shadowgraphy images of the laser-induced filaments (in the bulk of the carrier) and plasma (at the surface of the carrier), when the location (indicated by the white dashed line) of the focal spot is close to or inside the carrier. As was mentioned

Optics EXPRESS

in section 2, the shutter of the CCD camera was kept open during the entire process of the image capturing. Therefore, the evolution of the light, emitted from the laser-material interaction volume, cannot be resolved in time. Such light emissions (filaments in the bulk and plasma plumes on top of the carrier) can be observed in Fig. 4.

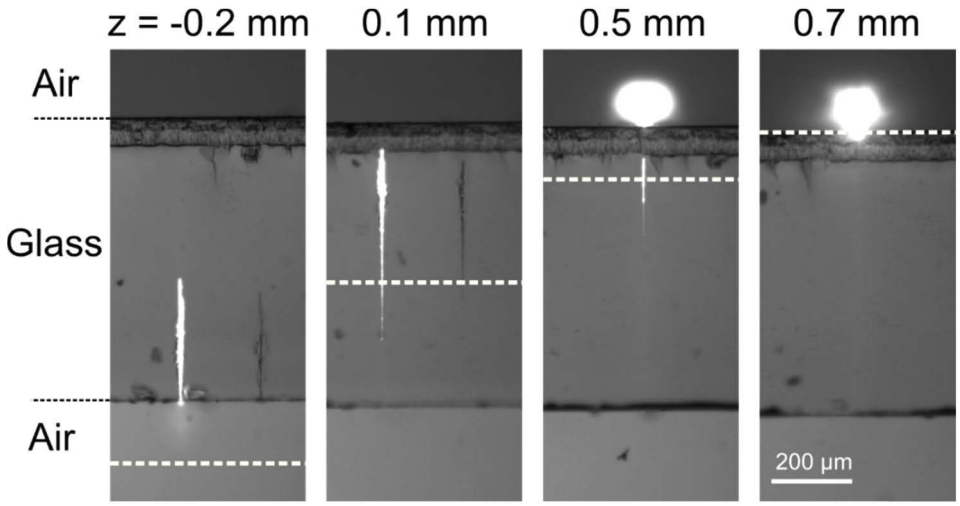

Fig. 4. Shadowgraphy images of the laser-induced filaments (in the bulk of the carrier) and the laser-induced plasma (on the top surface of the carrier). The white dashed line indicates the position of the focal spot of the laser beam. White "flashes" are the accumulated light of filamentation and the plasma expansion. Dark "filaments" were formed by previous laser pulses.

From these shadowgraphy images it can be concluded that the light, captured by PD2 originates from plasma generated at the top surface of the carrier. When the focal position was bellow $z = -0.2$ mm no plasma emissions were detected by PD2. This implies that, when the laser-induced damage occurred in the bulk of the carrier (at focal positions $z = -0.2$ mm and $z = 0.1$ mm in Fig. 4) no plasma emission was detected by PD2. From this analysis, the damage threshold of the soda-lime carrier was estimated to equal $F_{th} = 130 \pm 10$ J/cm^2. This value is close to the value reported in literature (116 J/cm^2) [38].

The remainder of this paper will focus only on the negative half (from $z = -7$ mm to $z = 0$) of the focus scan, since in this range of focal spot positions the laser-carrier interaction shows no light emission captured by PD2, see Fig. 3(d).

As can be observed in Fig. 3(d), when increasing the focal position from $z = -7$ mm, the signal of PD2 (black curve) starts to increase notably at about $z = -5.5$ mm in case of the standard LIFT configuration, while in the case of donor-up configuration such a "threshold focal position" is found at about $z = -3$ mm (red curve). These threshold focal positions correspond to peak fluence values of about $F_0 = 0.27$ J/cm^2 and $F_0 = 1$ J/cm^2, respectively. This implies that, a lower threshold and stronger signal of PD2 in case of the LIFT configuration (Fig. 3(a)), compared to the donor-up configuration (Fig. 3(b)) can therefore be attributed to spatial confinement of phenomena occurring at the carrier-donor interface in the case of the LIFT configuration (Fig. 3(a)). That is, in the LIFT configuration, the laser-donor interaction zone is spatially confined by the donor material underneath and the carrier glass above (Fig. 3(a)), while in donor-up configuration – the laser-donor interaction zone is only confined by the surrounding atmosphere towards the top, see Fig. 3(b). Characteristics of spatially confined plasma is reported by a number of research groups in LIBS, where the geometrical confinement is used in order to enhance the LIBS signal [39–41]. Such enhancement is explained by the laser-induced plasma

Optics EXPRESS

plume interacting with the shockwave, reflected by the confining surface [42]. The absorbed laser pulse initiates an expanding plasma plume as well as a shock wave. The latter travels upward, but is reflected back towards the donor from the confining element surface (the carrier in the case of the LIFT configuration). The reflected shockwave compresses the plasma plume into a smaller volume, increasing the collision rate of the plasma particles. In turn, this results in an increase of the plasma temperature—i.e. more atoms in a high(er)-energy states-, and as a consequence an enhanced emission intensity of the plasma [42]. Also Li et al. showed the increase of the plasma temperature and lifetime when the plasma is spatially confined [43]. Gao et al. showed that, as the distance to the confining surface increases, the enhancement of the emission reduces [44]. In the case of the standard LIFT configuration, the carrier substrate serves as a confining element, which reflects the shockwave, induced in the donor. Therefore, the plasma signal is stronger in the case of the standard LIFT configuration, than in the case of the donor-up configuration. Furthermore, analysis of the shadowgraphy images shown in Fig. 5 indicates that the focal positions where the jet-on-jet effect appears in a range from around $z = -5.5$ mm to -1.4 mm, corresponding to a spot diameter of 430 µm ($F_0 = 0.27$ J/cm^2) and of 100 µm ($F_0 = 5.1$ J/cm^2) on the donor surface, respectively. Since the focal position $z = -5.5$ mm is the threshold value at which the emission enhancement by the confinement effect and where jet-on-jet effect starts, the laser-induced plasma plume compressed by the reflected shock wave can explain the secondary jet ejection.

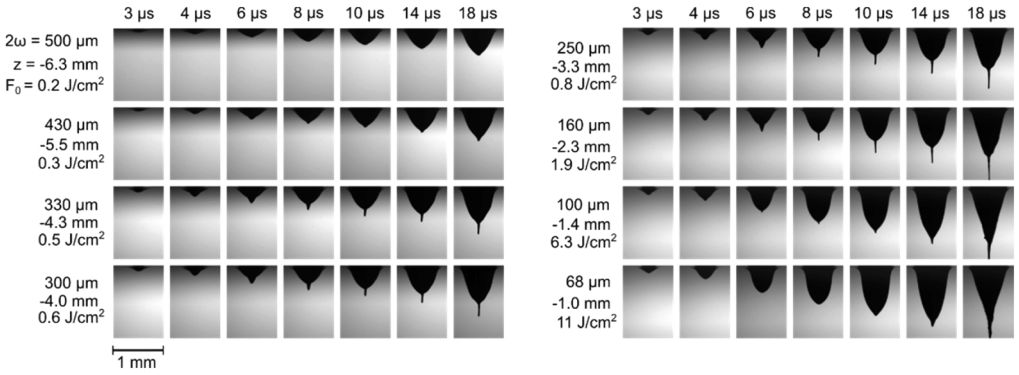

Fig. 5. Time-resolved shadowgraphy images of LIFT ejections as function of focal positions at a fixed laser pulse energy of $E_p = 200$ µJ. To the left of every shadowgraphy image sequence, the top value indicates the laser beam diameter (at $1/e^2$ of the peak intensity level) on the donor surface, middle – focal position (z), bottom corresponding peak fluence (F_0) on the donor surface. Negative z values indicates a beam focal position below the carrier/donor interface.

In order to investigate how laser-induced damage at the bottom surface of the carrier, as observed in Fig. 4 ($z = -0.2$ mm), correlates to the signal of photodiode PD2 in Fig. 3 and the images in Fig. 5, the carrier surface was cleaned after the experiments and subsequently inspected using optical and confocal microscopy, see Fig. 6.

Figure 6(a) shows shadowgraphy images of the jet-on-jet formation, whereas Fig. 6(b) shows corresponding optical (Fig. 6(b)) and extracted profiles from confocal (Fig. 6(c)) microscope images of the carrier. In order to show the presence of the secondary jet, a single shadowgraphy image from each sequence was selected at the instance of the maximum volume of the main LIFT ejection. This time instance corresponds to the transition from the first stage of bubble growth to the second stage of bubble collapse. At this time instance the secondary jet (if present) is already collapsed and elongating. When increasing the focal position from negative z-values to $z = 0$, the laser beam diameter on the carrier-donor interface reduces, the peak fluence F_0 increases and, as

Optics EXPRESS

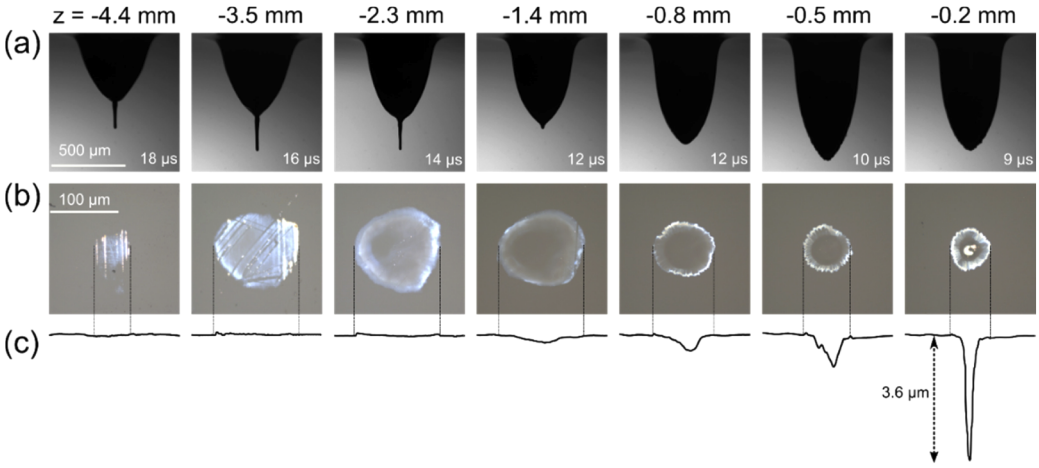

Fig. 6. (a) Shadowgraphy images of the LIFT ejections, captured at the time instance of the maximum volume of the main LIFT ejection, with indicated delays. (b) Optical microscope images of the carrier glass surface, modified by the laser-induced plasma during the LIFT process. (c) Confocal microscope profiles. Optical microscopy images and confocal profiles correspond to shadowgraphy images (a). The z-values on top indicate the focal position.

a result, the main LIFT ejection evolves faster in time. Therefore, the time delay where the main LIFT ejection starts collapsing reduces, see Fig. 6.

It was found that the focal position (threshold) at which the carrier deformation starts to occur is about $z = -4.4$ mm, which corresponds to $F_0 = 0.45$ J/cm^2 peak fluence, see Fig. 6(b). However, in the carrier-only configuration, the focal threshold position at which deformation occurs at the bottom of the carrier, equals at $z = -0.2$ mm, corresponding to $F_0 = 130$ J/cm^2. Such a significant difference in peak fluence, between 0.45 J/cm^2 and 130 J/cm^2 indicates that within the LIFT focus scan range from $z = -4.4$ mm to $z = -0.2$ mm, the deformation/damage of the bottom surface of the carrier does not occur because of the direct laser-carrier interaction. Instead, the carrier deformation is most likely caused by the laser-induced plasma, generated at the carrier-donor interface. That is, when focal position is $z = -4.4$ mm ($F_0 = 0.45$ J/cm^2), the laser-induced plasma reaches a temperature, which suffices to melt a thin layer of the carrier bottom surface. As the laser spot diameter on the donor surface is being further reduced, the area where the donor is exposed to a fluence $F_0 = 0.45$ J/cm^2, or higher, expands and the molten area on the carrier surface increases, see Fig. 6(b). Once the focal position reaches $z = -1.4$ mm ($F_0 = 5.6$ J/cm^2), a "crater" forms in the molten carrier surface, see Fig. 6(c). A similar crater formation was reported by Veiko et al. in laser-induced microplasma (LIMP) experiments [45]. In LIMP, the absorbing layer underneath the glass is used to generate laser-induced plasma, which is employed to structure the glass surface. The focal position $z = -1.4$ mm is the upper threshold at which the jet-on-jet effect is barely visible, see Fig. 6(a). The crater formation could be explained by the laser-induced shockwave impacting the carrier surface, molten by the high-temperature laser-induced plasma, and forming a crater instead of being reflected back into the plasma plume. If the shockwave is not reflected back, the plasma plume is not compressed and the secondary jet diminishes.

The fact that the secondary jet is diminishing around $z = -1.4$ mm in the focus scan could also be attributed to the decreasing diameter of the laser spot on the donor surface. If this diameter is being reduced, the area on the carrier-donor interface, exposed to fluence higher than the laser-induced plasma threshold will increase. At the same time, the area, exposed to fluence higher than the threshold of the main bubble ejection, will shrink. In this way, at certain focal

Optics EXPRESS

position of the focus scan these two areas will completely overlap each other and contribute to the same single ejection. In order to estimate the diameters of these areas, the threshold fluence values of both main and secondary ejections need to be determined.

The fluence threshold of the main ejection was estimated by extending the focus scan to the negative direction and estimating the laser spot diameter on the carrier-donor interface, where the smallest visible displacement of the donor/bubble is captured via the shadowgraphy imaging. This diameter was found to equal $2\omega = 1400$ µm, corresponding to a peak fluence $F_0 = 0.02$ J/cm^2. The similar approach was taken in order to estimate the fluence threshold of the secondary jet formation, which was found to equal $2\omega = 450$ µm, corresponding to a peak fluence $F_0 = 0.25$ J/cm^2. For every focal position, the diameter of the area above these threshold fluence values were calculated. An example of such calculation for the $z = -4$ mm ($2\omega = 300$ µm) is shown in Fig. 7(a), where the green line (also indicated by arrows in this graph) marks the diameter of the area "responsible" for the secondary ejection. In the same graph the red line (also indicated with arrows) marks the diameter of the area "responsible" for the main ejection. The diameters of the main (red circles) and the secondary (green triangles) ejection areas for every focal spot position are plotted in Fig. 7(b). This graph also shows the depth of craters, formed at the surface of the carrier (blue hollow squares), as well as diameters of the main ejection (black squares). These diameters were determined using an optical microscope and observing the donor through the carrier glass, after conducting the focal scan on a 2 µm thick donor layer. A relatively thin donor layer was selected in order to eliminate the bubble expansion effects and to accurately measure the area which was delaminated by the laser beam. It can be observed in Fig. 7(b), that the measured and calculated diameter values match well within the error bars. Furthermore, at the focal spot position at which the jet-on-jet effect diminishes ($z = -1.4$ mm), the diameters of the main and secondary jet ejection areas become almost equal in size – at about 150 µm. This implies that at this focal spot position, the main bubble (generated by the solvent evaporation) and the secondary bubble (generated by the laser-induced plasma plume) "overlap" and cannot be distinguished from each other. This is likely to play a role in the secondary jet diminishing, together with the crater formation on the carrier surface by the laser-induced shockwave.

Figure 7(c) shows the light intensity, captured by the PD2, and ejection speed as function of the focal spot position. The ejection speed was taken as the average of the bubble front speed during the expansion stage, since it was then found to be constant. It can be concluded from this figure that, as the diameter of the laser spot on the donor surface reduces, the fluence increases and the ejection speed increases. The speed shows a sharp drop at the focus position $z = -0.2$ mm, where the laser beam directly damages the carrier and, as a result, less energy is available to eject the donor material, see Fig. 4. However, the light intensity, captured by PD2 starts to decline at $z = -1.4$ mm, where the secondary jet diminishes. The diminishing of the secondary jet and the decline of the plasma signal can therefore be related to the crater formation on the bottom surface of the carrier. As the laser fluence increases, the laser-induced shockwave becomes strong enough to form a crater in the molten carrier surface, instead of being reflected from the carrier towards the donor. In that case, the compression of the laser-induced plasma plume, as mentioned above, reduces. That is, laser-induced plasma emission is not enhanced and the secondary jet does not longer occur.

Based on these results the effects occurring at various focal positions can be divided into five distinct focal regions, where different physical phenomena occur (see Fig. 8 and also Fig. 7(b)):

Region 1: $z < -5.5$ mm ($F_0 < 0.27$ J/cm^2) – In this region a single LIFT jet is ejected due to the expansion and collapse of the laser-induced high temperature and high pressure gas bubble. No effect of the laser-induced plasma or shock wave on the LIFT jet dynamics is present.

Region 2: -5.5 mm $< z < -4.4$ mm (0.27 J/cm^2 $< F_0 <$ 0.43 J/cm^2) – In this relatively narrow region a main jet is formed due to the classical bubble growth and collapse model. Moreover, at the high intensity center part of the beam a laser-induced plasma plume and a shock wave are

Optics EXPRESS

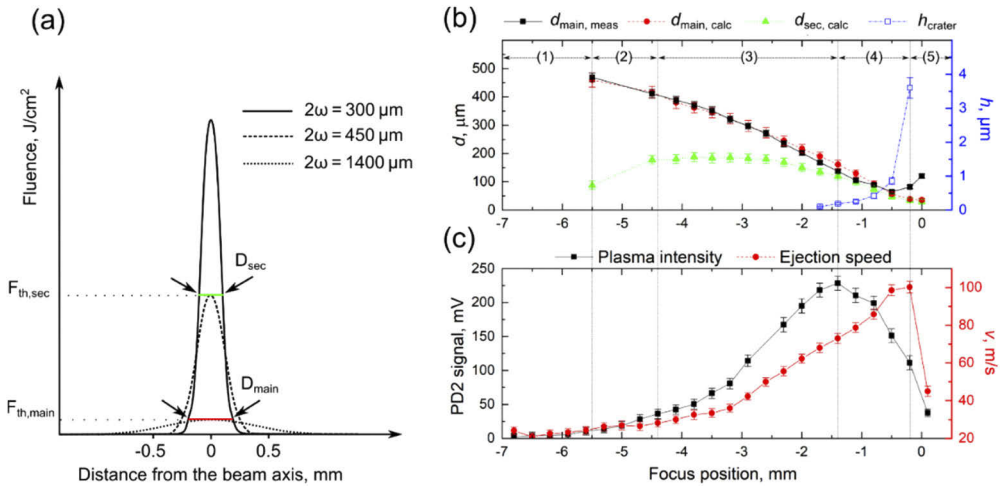

Fig. 7. (a) Gaussian fluence distributions at fixed pulse energy $E_p = 200$ μJ and 3 different size beam diameters: 300 μm, 450 μm, 1400 μm. Green line marks the diameter of the area "responsible" for the secondary and red – for main ejections (also indicated with arrows) (b) Calculated and measured (in case of main ejection) diameters and craters depth dependencies on the focus scan position. (c) The light emitted by the plasma, as captured by the PD2, and ejection speed, as function of the focus scan position. Different regimes in (a-b) are explained in Fig. 8.

generated. The latter is reflected from the carrier surface and travels backwards, compressing the volume and increasing the pressure of the plasma plume, as well as the emission intensity. This results in the formation of the small secondary bubble on top of the main bubble. As the volume of the latter grows, the high pressure gas diffuses from the secondary into the main bubble. Because of this relatively rapid pressure drop, the secondary bubble collapses forming a small jet on top of the main bubble, which continues growing. In this region, the temperature of the laser-induced plasma is not high enough to melt the carrier surface.

Region 3: -4.4 mm $< z < -1.4$ mm (0.43 J/cm$^2 < F_0 < 5.1$ J/cm^2) – Here the same jet-on-jet ejection is observed as in the previous region. However, the temperature of the laser induced plasma becomes high enough to melt a thin layer of the carrier surface.

Region 4: -1.4 mm $< z < -0.2$ mm (5.1 J/cm$^2 < F_0 < 120$ J/cm^2) – In this region the carrier surface is not only molten by the laser-induced plasma, but the shock wave becomes strong enough to form a crater at the carrier surface, see blue hollow squares in Fig. 7(b). Furthermore, in this region the emission of the laser-induced plasma decreases, this can be seen in Fig. 7(b). This suggests that the fluence reaching the donor surface drops. However, within the same region the LIFT jet speed increases. Such counter-intuitive behavior can be, firstly, explained by the shock wave interaction with the carrier surface. When the focus position exceeds -1.4 mm, the significant portion of a shock wave energy is consumed to form a crater in the molten carrier surface. This limits its capacity to be reflected backwards to the plasma plume, which would have enhanced the emission and form the secondary jet. Secondly, the diameters of the main and the secondary ejection areas become almost equally sized. Therefore, the secondary ejection cannot be distinguished from the main ejection.

Region 5: $z > -0.2$ mm ($F_0 > 120$ J/cm^2) – In Fig. 7(b), a sudden jump of the crater depth can be observed from $z = -0.5$ mm to $z = -0.2$ mm. This occurs because the laser fluence penetrating the carrier becomes high enough to directly damage it. At this point, the speed of the jet starts to decrease, as the part of the laser energy is lost due to the non-linear absorption of the glass

Optics EXPRESS

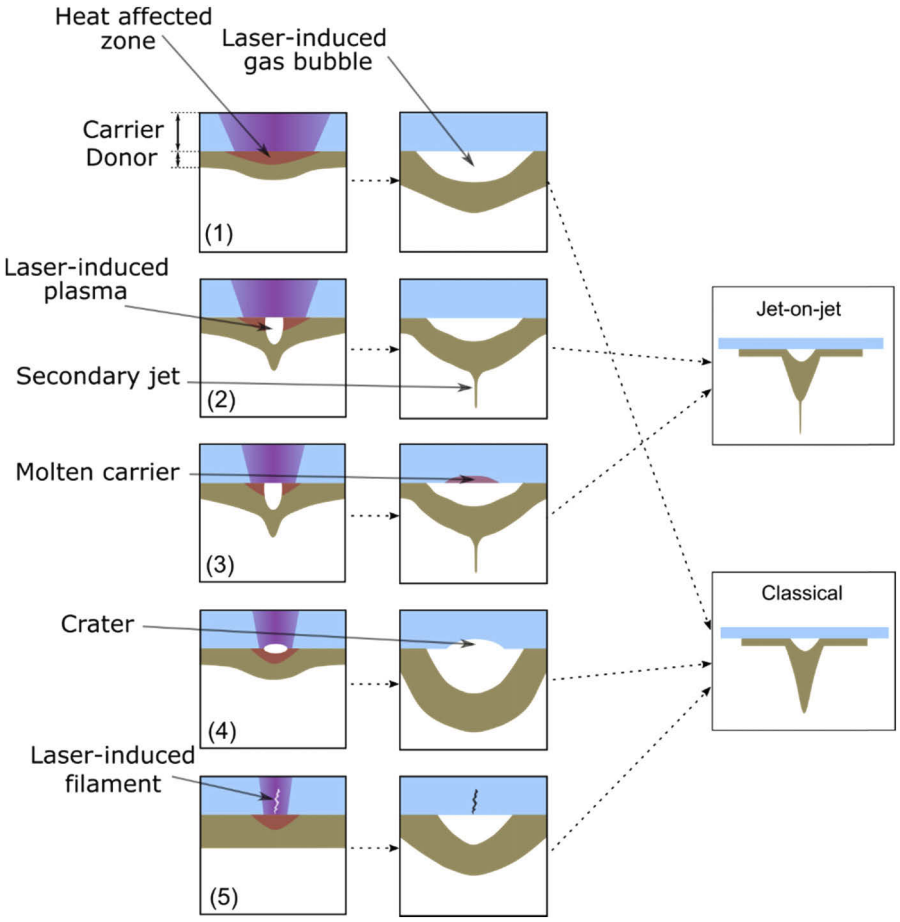

Fig. 8. Schematic of the evolution of the jet-on-jet formation with 5 scenarios depending on the region of the focal position z.

carrier. As the focal position is moved upwards, the laser-induced damage inside the carrier follows, see Fig. 4.

The jet-on-jet phenomenon described in focal regions 2 and 3 shows a small(er) secondary jet generated by the laser-induced plasma, on top of the main jet, generated by the gas bubble expansion. Although due to this phenomenon a substantial decrease in jet widths can be observed in Fig. 5, our presented and discussed jet-on-jet ejection mechanism can not be directly exploited in order to print small(er) deposits over large(r) printing distances. That is due to the fact, that both physical phenomena responsible for the main jet (induced by gas bubble expansion) and the secondary jet (induced by laser-induced plasma) are triggered by a single laser beam, and therefore can not be controlled independently. However, the small(er) secondary jet could be generated using a second (coaxial) laser beam, whose diameter and fluence level is controlled independently from the main laser beam, used to generate the main big(er) ejection. This way, the ejection diameters and fluence levels could be selected independently: (1) a laser beam with a large spot diameter and a low fluence level is used to generate a jet, which will not induce enough material flow in order to cover the printing distance; (2) a laser beam with small spot diameter and high(er) fluence, which is focused in the center of the large diameter beam, in order to eject a narrow jet, which would be “carried” to the receiver substrate by the large jet. Such double-beam

Optics EXPRESS

LIFT approach will be addressed in future studies, where we will focus on the realization and optimization of the jet-on-jet inspired deposition mechanism, described above.

4. Conclusions

In this work, the new phenomenon of jet-on-jet LIFT ejection was reported. In order to understand the impact of the processing parameters on this effect, a focus scan was conducted. Time-resolved shadowgraphy imaging was used to capture jetting dynamics and a fast photodiode was used to capture laser-induced plasma emissions. It was found that the focus position where the jet-on-jet effect is visible matches with the focus location, at which the plasma emission is enhanced by the carrier glass confinement of the plasma. This was attributed to the plasma plume compression by the shockwave, induced in the donor material, which is subsequently reflected by the carrier surface. The focus position at which the jet-on-jet effect diminishes was found to match the focal location at which a crater in the carrier surface is formed and the plasma emission intensity starts to decrease. This observation is explained by the energy loss of the shock wave due to the formation of a crater in the carrier, instead of being reflected, enhancing plasma emission and inducing the secondary jet.

New insights in the physics governing of the LIFT of silver nanoparticle ink ejection mechanism were found. That is, where laser-induced plasma expansion and shockwave is responsible for the ejection in LIFT of solids and the gas bubble generation in LIFT of liquids, the combination of two play a role in LIFT of silver nanoparticle inks. Since the secondary jet shows a smaller diameter than the main jet, the jet-on-jet effect could potentially be exploited for higher resolution printing, when compared to the use of the main jet only. In a future study we will trigger the secondary jet using a second, tightly focused laser beam, which will allow the control of the two ejection mechanisms independently.

Funding

Nederlandse Organisatie voor Wetenschappelijk Onderzoek (14641).

Acknowledgements

The authors would like to thank Edsger Smits and Merijn Giesbers for technical support and mindful discussions.

Disclosures

The authors declare no conflicts of interest

References

1. M. Morales, D. Munoz-Martin, A. Marquez, S. Lauzurica, and C. Molpeceres, *Laser-Induced Forward Transfer Techniques and Applications*, Second Edi (Elsevier Ltd., 2017).
2. A. Pique and P. Serra, *Laser Printing of Functional Materials: 3D Microfabrication, Electronics and Biomedicine* (Wiley, 2018), Vol. 39.
3. D. Puerto, E. Biver, A. P. Alloncle, and P. Delaporte, "Single step high-speed printing of continuous silver lines by laser-induced forward transfer," Appl. Surf. Sci. **374**, 183–189 (2016).
4. P. Sopeña, J. Arrese, S. González-Torres, J. M. Fernández-Pradas, A. Cirera, and P. Serra, "Low-Cost Fabrication of Printed Electronics Devices through Continuous Wave Laser-Induced Forward Transfer," ACS Appl. Mater. Interfaces **9**(35), 29412–29417 (2017).
5. M. Zenou, A. Sa'Ar, and Z. Kotler, "Laser Transfer of Metals and Metal Alloys for Digital Microfabrication of 3D Objects," Small **11**(33), 4082–4089 (2015).
6. R. Pohl, C. W. Visser, G. W. Römer, D. Lohse, C. Sun, and B. Huis in 't Veld, "Ejection regimes in picosecond laser-induced forward transfer of metals," Phys. Rev. Appl. **3**(2), 024001 (2015).
7. C. Unger, J. Koch, L. Overmeyer, and B. N. Chichkov, "Time-resolved studies of femtosecond-laser induced melt dynamics," Opt. Express **20**(22), 24864 (2012).

Optics EXPRESS

8. D. Bartl, A. Michalowski, M. Hafner, A. Letsch, S. Nolte, and A. Tünnermann, "Time-resolved study of back side ablated molybdenum thin films by ultrashort laser pulses," Appl. Phys. A **110**(1), 227–233 (2013).
9. M. Feinaeugle, A. P. Alloncle, P. Delaporte, C. L. Sones, and R. W. Eason, "Time-resolved shadowgraph imaging of femtosecond laser-induced forward transfer of solid materials," Appl. Surf. Sci. **258**(22), 8475–8483 (2012).
10. K. S. Kaur, R. Fardel, T. C. May-Smith, M. Nagel, D. P. Banks, C. Grivas, T. Lippert, and R. W. Eason, "Shadowgraphic studies of triazene assisted laser-induced forward transfer of ceramic thin films," J. Appl. Phys. **105**(11), 113119 (2009).
11. M. Feinaeugle, D. J. Heath, B. Mills, J. A. Grant-Jacob, G. Z. Mashanovich, and R. W. Eason, "Laser-induced backward transfer of nanoimprinted polymer elements," Appl. Phys. A **122**(4), 398 (2016).
12. D. J. Heath, M. Feinaeugle, J. A. Grant-Jacob, B. Mills, and R. W. Eason, "Dynamic spatial pulse shaping via a digital micromirror device for patterned laser-induced forward transfer of solid polymer films," Opt. Mater. Express **5**(5), 1129 (2015).
13. M. Colina, M. Duocastella, J. M. Fernández-Pradas, P. Serra, and J. L. Morenza, "Laser-induced forward transfer of liquids: Study of the droplet ejection process," J. Appl. Phys. **99**(8), 084909 (2006).
14. D. A. Willis and V. Grosu, "Microdroplet deposition by laser-induced forward transfer," Appl. Phys. Lett. **86**(24), 244103 (2005).
15. M. Duocastella, J. M. Fernández-Pradas, J. L. Morenza, and P. Serra, "Sessile droplet formation in the laser-induced forward transfer of liquids: A time-resolved imaging study," Thin Solid Films **518**(18), 5321–5325 (2010).
16. A. Karaiskou, I. Zergioti, C. Fotakis, M. Kapsetaki, and D. Kafetzopoulos, "Microfabrication of biomaterials by the sub-ps laser-induced forward transfer process," Appl. Surf. Sci. **208-209**, 245–249 (2003).
17. M. Colina, P. Serra, J. M. Fernández-Pradas, L. Sevilla, and J. L. Morenza, "DNA deposition through laser induced forward transfer," Biosens. Bioelectron. **20**(8), 1638–1642 (2005).
18. L. Rapp, J. Ailuno, A. P. Alloncle, and P. Delaporte, "Pulsed-laser printing of silver nanoparticles ink: control of morphological properties," Opt. Express **19**(22), 21563 (2011).
19. D. Munoz-Martin, C. F. Brasz, Y. Chen, M. Morales, C. B. Arnold, and C. Molpeceres, "Laser-induced forward transfer of high-viscosity silver pastes," Appl. Surf. Sci. **366**, 389–396 (2016).
20. C. Boutopoulos, A. P. Alloncle, I. Zergioti, and P. Delaporte, "A time-resolved shadowgraphic study of laser transfer of silver nanoparticle ink," Appl. Surf. Sci. **278**, 71–76 (2013).
21. Y. Chen, D. Munoz-Martin, M. Morales, C. Molpeceres, E. Sánchez-Cortezon, and J. Murillo-Gutierrez, "Laser induced forward transfer of high viscosity silver paste for new metallization methods in photovoltaic and flexible electronics industry," Phys. Procedia **83**, 204–210 (2016).
22. T. Araki, R. Mandamparambil, D. M. P. Van Bragt, J. Jiu, H. Koga, J. Van Den Brand, T. Sekitani, J. M. J. Den Toonder, and K. Suganuma, "Stretchable and transparent electrodes based on patterned silver nanowires by laser-induced forward transfer for non-contacted printing techniques," Nanotechnology **27**(45), 45LT02 (2016).
23. E. Breckenfeld, H. Kim, R. C. Y. Auyeung, N. Charipar, P. Serra, and A. Piqué, "Laser-induced forward transfer of silver nanopaste for microwave interconnects," Appl. Surf. Sci. **331**, 254–261 (2015).
24. J. Wang, R. C. Y. Auyeung, H. Kim, N. A. Charipar, and A. Piqué, "Three-dimensional printing of interconnects by laser direct-write of silver nanopastes," Adv. Mater. **22**(40), 4462–4466 (2010).
25. A. Kalaitzis, M. Makrygianni, I. Theodorakos, A. Hatziapostolou, S. Melamed, A. Kabla, F. de la Vega, and I. Zergioti, "Jetting dynamics of Newtonian and non-Newtonian fluids via laser-induced forward transfer: Experimental and simulation studies," Appl. Surf. Sci. **465**, 136–142 (2019).
26. C. Boutopoulos, I. Kalpyris, E. Serpetzoglou, and I. Zergioti, "Laser-induced forward transfer of silver nanoparticle ink: Time-resolved imaging of the jetting dynamics and correlation with the printing quality," Microfluid. Nanofluid. **16**(3), 493–500 (2014).
27. C. Florian, F. Caballero-Lucas, J. M. Fernández-Pradas, R. Artigas, S. Ogier, D. Karnakis, and P. Serra, "Conductive silver ink printing through the laser-induced forward transfer technique," Appl. Surf. Sci. **336**, 304–308 (2015).
28. Z. Zhang, R. Xiong, R. Mei, Y. Huang, and D. B. Chrisey, "Time-Resolved Imaging Study of Jetting Dynamics during Laser Printing of Viscoelastic Alginate Solutions," Langmuir **31**(23), 6447–6456 (2015).
29. M. Duocastella, J. M. Fernández-Pradas, J. L. Morenza, and P. Serra, "Time-resolved imaging of the laser forward transfer of liquids," J. Appl. Phys. **106**(8), 084907 (2009).
30. C. Unger, M. Gruene, L. Koch, J. Koch, and B. N. Chichkov, "Time-resolved imaging of hydrogel printing via laser-induced forward transfer," Appl. Phys. A **103**(2), 271–277 (2011).
31. E. Biver, L. Rapp, A. Alloncle, and P. Delaporte, "Applied Surface Science Multi-jets formation using laser forward transfer," Appl. Surf. Sci. **302**, 153–158 (2014).
32. . "Sicrys P75DB-1 - PvNanoCell," https://www.pvnanocell.com/sicrys-p75db-1.html.
33. J. Mikšys and G. A. G. R. B. E. Römer, "Pico- to nanosecond pulsed laser-induced forward transfer (LIFT) of silver nanoparticle inks: a comparative study," Appl. Phys. A **125**(12), 814 (2019).
34. J. König, S. Nolte, and A. Tünnermann, "Plasma evolution during metal ablation with ultrashort laser pulses," Opt. Express **13**(26), 10597 (2005).
35. L. M. Cabalin and J. J. Laserna, "Experimental determination of laser induced breakdown thresholds of metals under nanosecond Q-switched laser operation," Spectrochim. Acta, Part B **53**(5), 723–730 (1998).

Optics EXPRESS

36. A. De Giacomo, R. Gaudiuso, C. Koral, M. Dell'Aglio, and O. De Pascale, "Nanoparticle Enhanced Laser Induced Breakdown Spectroscopy: Effect of nanoparticles deposited on sample surface on laser ablation and plasma emission," Spectrochim. Acta, Part B **98**, 19–27 (2014).
37. A. De Giacomo, R. Gaudiuso, C. Koral, M. Dell'Aglio, and O. De Pascale, "Nanoparticle-enhanced laser-induced breakdown spectroscopy of metallic samples," Anal. Chem. **85**(21), 10180–10187 (2013).
38. D. Nieto, J. Arines, G. M. O'Connor, and M. T. Flores-Arias, "Single-pulse laser ablation threshold of borosilicate, fused silica, sapphire, and soda-lime glass for pulse widths of 500 fs, 10 ps, 20 ns," Appl. Opt. **54**(29), 8596 (2015).
39. X. K. Shen, J. Sun, H. Ling, Y. F. Lu, X. K. Shen, J. Sun, H. Ling, and Y. F. Lu, "Spatial confinement effects in laser-induced breakdown spectroscopy Spatial confinement effects in laser-induced breakdown spectroscopy," Appl. Phys. Lett. **91**(8), 081501 (2007).
40. Y. Fu, Z. Hou, and Z. Wang, "Physical insights of cavity confinement enhancing effect in laser-induced breakdown spectroscopy," Opt. Express **24**(3), 3055–3066 (2016).
41. A. M. Popov and R. Fantoni, "Enhancement of LIBS signal by spatially confining the laser-induced plasma," J. Anal. At. Spectrom. **24**(5), 602–604 (2009).
42. Y. Qiu, C. Yao, C. Yao, J. Gan, W. Zhang, N. Xu, J. Sun, and J. Wu, "Spatial confinement of laser-induced plasma by laser-induced and obstacle-reflected shock wave and its effect on optical emission of laser-induced plasma," AIP Adv. **9**(9), 095021 (2019).
43. C. Li, J. Wang, and X. Wang, "Shock wave confinement-induced plume temperature increase in laser-induced breakdown spectroscopy," Phys. Lett. A **378**(45), 3319–3325 (2014).
44. X. Gao, L. Liu, C. Song, and J. Lin, "The role of spatial confinement on nanosecond YAG laser-induced Cu plasma," J. Phys. D: Appl. Phys. **48**(17), 175205 (2015).
45. V. P. Veiko, S. A. Volkov, R. A. Zakoldaev, M. M. Sergeev, A. A. Samokhvalov, G. K. Kostyuk, and K. A. Milyaev, "Laser-induced microplasma as a tool for microstructuring transparent media," Quantum Electron. **47**(9), 842–848 (2017).